

RESEARCH ARTICLE

Open Access



A 3D approach to reconstruct continuous optical images using lidar and MODIS

HuaGuo Huang* and Jun Lian

Abstract

Background: Monitoring forest health and biomass for changes over time in the global environment requires the provision of continuous satellite images. However, optical images of land surfaces are generally contaminated when clouds are present or rain occurs.

Methods: To estimate the actual reflectance of land surfaces masked by clouds and potential rain, 3D simulations by the RAPID radiative transfer model were proposed and conducted on a forest farm dominated by birch and larch in Genhe City, DaXing'AnLing Mountain in Inner Mongolia, China. The canopy height model (CHM) from lidar data were used to extract individual tree structures (location, height, crown width). Field measurements related tree height to diameter of breast height (DBH), lowest branch height and leaf area index (LAI). Series of Landsat images were used to classify tree species and land cover. MODIS LAI products were used to estimate the LAI of individual trees. Combining all these input variables to drive RAPID, high-resolution optical remote sensing images were simulated and validated with available satellite images.

Results: Evaluations on spatial texture, spectral values and directional reflectance were conducted to show comparable results.

Conclusions: The study provides a proof-of-concept approach to link lidar and MODIS data in the parameterization of RAPID models for high temporal and spatial resolutions of image reconstruction in forest dominated areas.

Keywords: Lidar; Optical; Temporal interpolation; 3D model; High resolution

Background

Optical remote sensing images have been widely used in monitoring forest ecosystems. Spatial, temporal and spectral resolutions are the three key indicators to be considered during most applications. Spatial resolution had been improved from a scale of hundreds of meters (e.g. Landsat 8) to one of a half-meter (e.g. GeoEye-1 or Worldview-2) with only a slight increase in the number of spectral bands. However, in forested area, temporal resolution is generally reduced by frequent rains or cloud covers, which prevents users from continuously acquiring clear optical remote sensing images.

Temporally continuous satellite images are important for forest monitoring (Lunetta et al. 2004; Masek et al. 2008; Nitze et al. 2015) since forest reflectance varies with seasonality (Kobayashi et al. 2007; Xu et al. 2013).

A few studies have been conducted to interpolate those contaminated images by rains or clouds. For example, Landsat images have been blended with MODerate-resolution Imaging Spectroradiometer (MODIS) data to create spatial and temporal fusion data (Gao et al. 2006; Hilker et al. 2009; Wu et al. 2012). Further, radiative transfer models have also been used to simulate a series of high temporal resolution images for future space earth observation missions (Inglada et al. 2011). However, spatial resolution is generally moderate due to the use of simple homogeneous radiative transfer models, which are not able to deal with high resolution simulation with diverse tree species and mountain shadows.

In recent years, light detection and ranging (lidar) has been a widely used tool for forest studies (Adams et al. 2012; Arno et al. 2013; Montesano et al. 2013). The greatest advantage of lidar is to provide direct measurements of very detailed 3D forest structures, so it can be used to reconstruct 3D trees to support the simulation

* Correspondence: huaguo.huang@gmail.com
Key Laboratory for Silviculture and Conservation of Ministry of Education,
Beijing Forestry University, Beijing, China

of radar remote sensing signals (Lucas et al. 2006) and to study how 3D structures affect the quality of optical images (Barbier et al. 2011). By coupling lidar with high temporal data such as MODIS using 3D radiative transfer models, it will be possible to generate both high spatial and temporal resolution optical remote sensing images. However, very few studies were found using this approach. Therefore, we will test the possibility of that approach to simulate high-resolution optical satellite images on an arbitrary day of the growing season in a forested area.

Methods

Study site

The study site (Fig. 1), located in a 100 ha forested area (50°54' N, 121°54' E) of the Genhe Forestry Reserve, DaXing'AnLing Mountain in Inner Mongolia, China, belongs to a boreal moist and cold temperature forest, with an elevation ranging from 784 to 1142 m. Annual average precipitation is 450 to 550 mm, with sixty per cent falling in July and August. Annual average sunshine is 2594 h with a frost-free period of 80 days. Our study site occupied 75 % of the total area. The forest is mainly composed of Dahurian Larch (*Larix gmelinii*) and White Birch (*Betula platyphylla* Suk.). The understory vegetation of the larch forest is a single layer of evergreen shrubs (normally *Ledum palustre* L. or *Rhododendron dauricum* L.). *L. palustre* is generally a low shrub (less than 0.3 m), while the height of *R. dauricum* is around 1.5 m. Blueberries (*Semen trigonellae*) are widely distributed. The birch forest has a understory of grass or deciduous shrubs, such as *Rosa acicularis*, *Spiraea sericea* Turcz., or *Rubus* L.

The growing season typically begins in early May and senescence occurs in late September. In the summer of 2013, 18 field plots (45 m by 45 m) were established representing different combinations of forest types, density and leaf area index (LAI) (Table 1). The LAI, ranging from 1.44 to 3.51 m²·m⁻², was measured using LAI-2000 (LICOR Inc.) hemispheric data. The forest cover varies between 0.21 and 0.86.

Based on inventory data of individual tree structures in plots L1 to L9, the DBH and crown length (*L*) of trees were regressed on tree height (*H*), where heights were derived by lidar. For convenience, both crowns of larch and birch are defined as spherical in shape.

Reflectance or transmittance spectra of leaves, branches and stems of birch and larch trees were measured in the field using the integrating sphere of ASD (Analytical Spectral Device, <http://www.asdi.com/>). Dry and wet soil spectra were the default soil spectra in a PROSAIL model (Jacquemoud et al. 2009). The re-sampled spectral curves are shown in Fig. 2.

Airborne data

Small footprint full-waveform lidar data were acquired from August 16 to September 25 in 2012 (Mu et al. 2015). The system consisted of a Leica ALS60 with an integrated Leica RCD105 camera. The CCD camera produced natural color mosaic images with 0.2 m resolution. As for lidar, the mean swath width was 1 km at a flying altitude of approximately 2700 m (over rough terrain). The scan angle was less than 35°. Waveforms were digitized with a frequency of 100 to 200 kHz. An average of eight reflected pulses per m² was obtained over the sample plots. Point

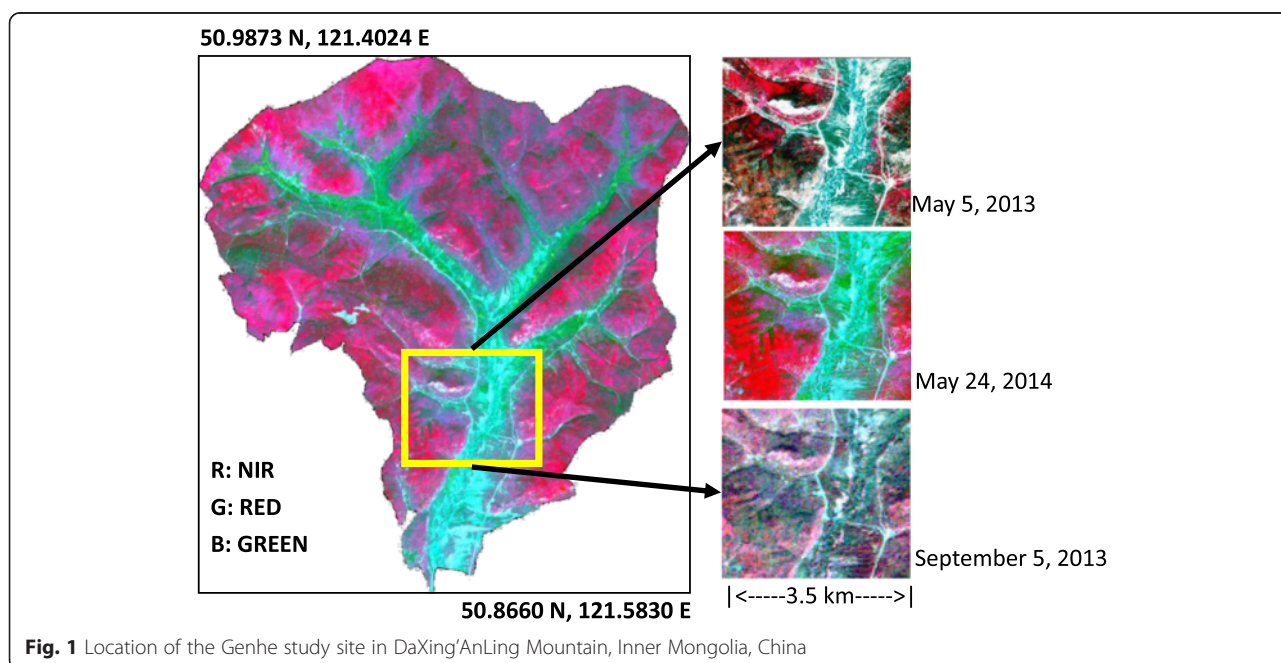


Table 1 Plot variables at the study site

Stand ID	Tree stems (Birch: Larch)	Slope (°)	Shrub height (m) and cover	Mean tree height (m)	Mean DBH (cm)	LAI (m ² ·m ⁻²)
A1	83:140	35	1.5, 70 %	11.6	11.8	2.68 ± 0.13
A2	97: 248	20	1.8, 60 %	12.1	11.6	2.88 ± 0.24
A3	41:269	25	1.5, 75 %	11.0	11.4	2.56 ± 0.09
A4	174:22	5	0.7, 3 %	16.0	16.1	3.31 ± 0.07
A5	142:103	10	2.0, 80 %	11.8	11.8	No data
A6	91:173	45	0.3, 80 %	11.2	11.5	No data
A7	111:102	30	1.5, 50 %	14.2	16.2	2.06 ± 0.13
A8	156:238	10	No data	11.0	9.5	2.51 ± 0.20
A9	65:180	45	1.3, 70 %	14.5	15.4	2.36 ± 0.17
L1	131:220	5	1.2, 20 %	8.4	10.0	2.71 ± 0.25
L2	89:421	<5	1.2, 5 %	9.0	8.7	3.06 ± 0.22
L3	11:71	5	0.7, 3 %	8.0	7.8	2.42 ± 0.50
L4	294:79	5	1.2, 15 %	11.7	11.6	3.51 ± 0.20
L5	1:327	7	1.0, 5 %	12.5	12.9	2.43 ± 0.12
L6	0:173	5	0.5, 20 %	17.2	22.3	1.44 ± 0.06
L7	11:90	7	1.0, 80 %	9.7	12.5	1.50 ± 0.15
L8	60:118	12	1.3, 30 %	13.1	15.4	2.70 ± 0.12
L9	0:585	5	0.5, 50 %	8.4	8.7	2.28 ± 0.09

clouds were first classified by the TerraScan software (see www.terrasolid.com) to separate the ground points from other points. We used Delaunay triangulation and bilinear interpolation method to generate a digital elevation model (DEM) from ground returns. DSM (digital surface model) was created using a maximum value in a window size of 0.5 m. CHM (canopy height model) was calculated as the difference between DSM and DEM (Fig. 3).

Individual tree crowns were segmented from CHM using the “TreeVaW” tool (Popescu and Wynne 2004), which uses a circular window filter to segment trees and produces the location of each tree (x_i, y_i), height (H_i) and crown radius (R_i).

Optical satellite images

Several scales of geo-referenced satellite images were used, including SPOT-6 (1 m), Landsat (30 m) and MODIS (250 m). Due to frequent cloud cover, SPOT and Landsat were not able to capture clear land surface images during rainy days, which happened mostly in the growing season (May to September). There was only one cloud-free SPOT-6 image, obtained on October 10, 2013. For the same reason, only three Landsat images were clear (May 5, 2013; Sep 9, 2013; Sep 29, 2013) in 2013. As well, we collected a Landsat 8 image on May 24, 2014.

A Gram-Schmidt Spectral Sharpening image fusion technique in ENVI 5.1 (ITT Exelis) was applied to produce

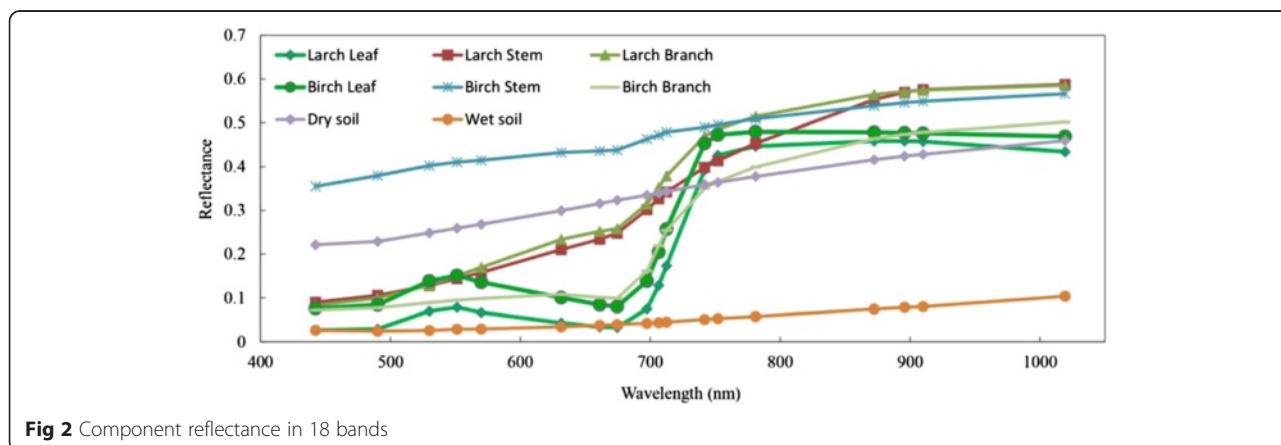


Fig 2 Component reflectance in 18 bands

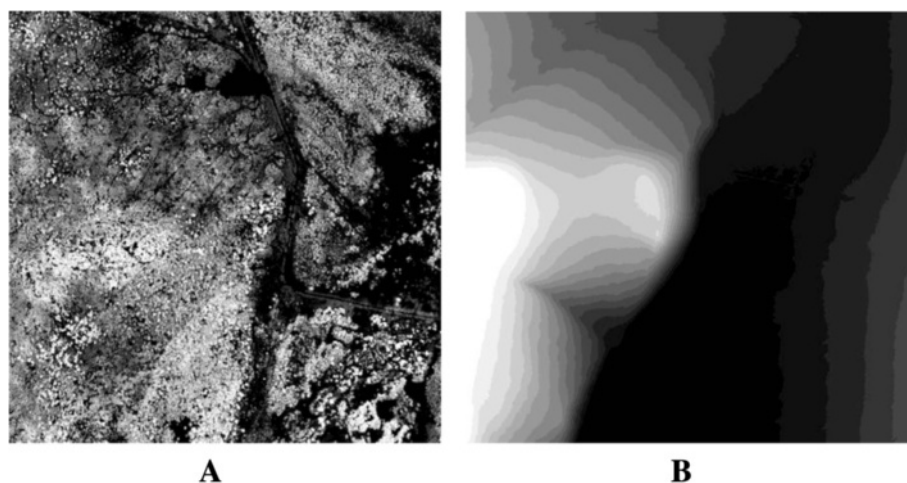


Fig. 3 Lidar derived CHM and DEM (1 km): **a** CHM, gray color representing tree height 0–30 m; **b** DEM, gray color representing elevation 770–895 m

pan-sharpened Landsat 7 or 8 multi-spectral images with a resolution of 15 m. This pan-sharpening method was selected because it preserves the original spectral information of the image and can be simultaneously applied to multi-spectral bands. The Landsat image pixel values (in digital numbers) were converted to top-of-atmosphere (TOA) spectral radiance, which was further converted to land surface reflectance using the Fast Line-of-sight Atmospheric Analysis of Hypercubes (FLAASH) atmospheric correction model with the atmospheric visibility parameter estimated from the MODIS aerosol product.

MODIS 16-day 250 m NDVI images and the 500 m LAI products from Jan 1 to Dec 31, 2013 were downloaded. Because a maximum value filtering method was used, NDVI and LAI products had significantly fewer cloud cover problems. NDVI data were used to determine the phenology of the boreal forest, including birch, larch and understory, which allow interpolation of Landsat images ranging from clear to contaminated days. MODIS LAI products were utilized to determine the leaf area of each tree. Despite its low resolution, it is the only continuous global leaf area product, but with acceptable accuracy (Ahl et al. 2006).

MODIS Bidirectional Reflectance Factor (BRF) products in May of 2013 were collected for validation. The BRF curves were reconstructed from the kernel coefficients using the Algorithm for Model Bidirectional Reflectance Anisotropies of the Land Surface (AMBRALS) (Wanner et al. 1995; Huang et al. 2013b; Sharma et al. 2013).

RAPID model

RAPID is a 3D radiative transfer model, able to simulate reflectance images over complex 3D natural scenes at large scales (30 to 1000 m) with great efficiency (Huang et al. 2013a), implying that RAPID can simulate images

at MODIS pixel scales (250 to 1000 m). The main input parameters of RAPID consist of 3D structures of the ground, trees, buildings and rivers, as well as reflectance and transmittance of leaves, branches, walls, water bodies and roads under a few sun and sensor angles. The main outputs are BRF curves and land surface reflectance images with defined spatial resolution (default 0.5 m).

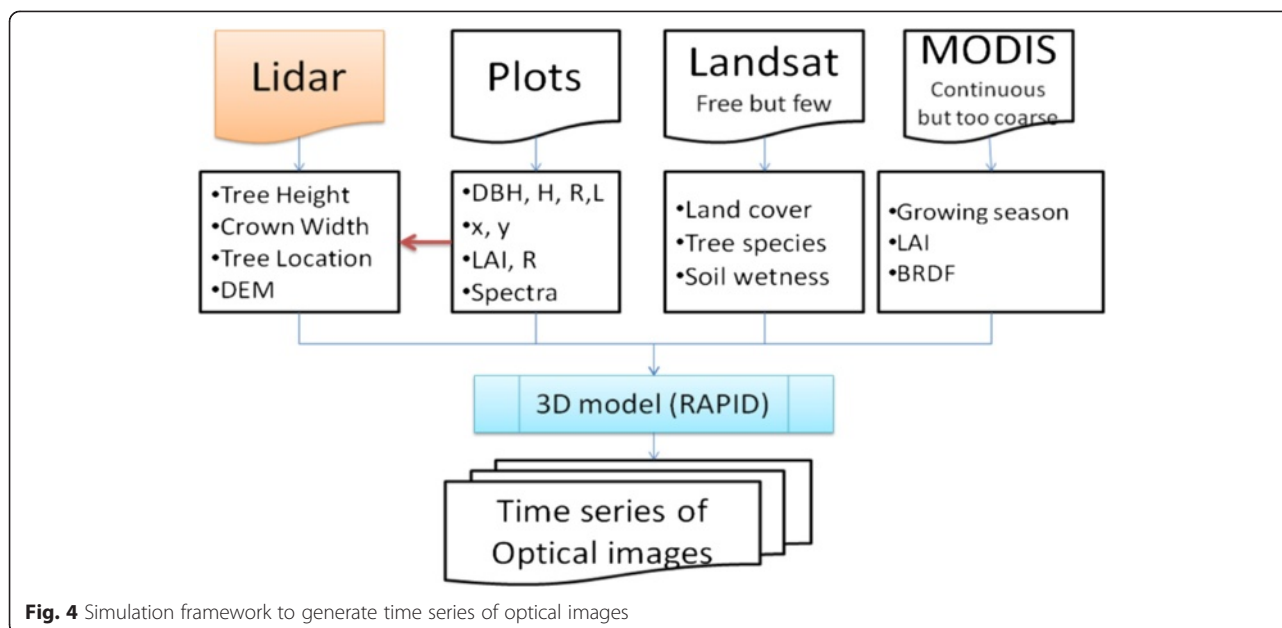
Simulation framework

Figure 4 shows the 3D simulation framework, with integrated parameters extracted from lidar data, field plots data, Landsat images and MODIS images managed into the RAPID model to simulate optical images of a virtual sensor with several view angles, 18 spectral bands and a half-meter spatial resolution.

The sensor is an advanced version of the Compact High Resolution Imaging Spectrometer (CHRIS/PROBA). CHRIS is the only multi-angular sensor launched with both high spatial (17 m) and spectral resolution (20–40 nm) (Rautiainen et al. 2008; García Millán et al. 2014). For any selected target, five images with different viewing angles (-55° , -36° , 0° , 36° and 55°) were made within a short span of 2.5 min. The virtual sensor was placed above the canopy under clear sky conditions.

A large number of input parameters needed to be set in order to simulate seasonal variation. A few parameters, such as LAI and soil moisture, vary considerably over the growing season, while other parameters remain relatively stable. Given our relatively limited data source, we defined five basic assumptions to reduce the number of unknowns:

- 1) The DTM (digital terrain model) remained unchanged, a reasonable assumption for forested areas;



- 2) Tree crowns were ellipsoid or cone shaped, similar with geometric optic models (Schaaf and Strahler 1994; Chen et al. 2012);
- 3) Individual tree LAI (LAI_{tree}) was predicted from tree height (Xiao et al. 2006);
- 4) We accepted a spherical leaf angle distribution (LAD_{tree}) for all trees due to missing measurements;
- 5) Reflectance of non-vegetation objects, such as walls, water bodies and roads remained constant, following precedents set in existing literature (Wang et al. 2008) or in the ENVI spectral library.

With these assumptions, there were two types of input parameters: fixed or dynamic. Fixed parameters were DEM, land cover map, individual tree map (coordinates, DBH, height, crown radius, crown length). DEM and land cover map were re-sampled to a resolution of 1 m. Land cover maps were generated using a decision tree method with six classes: bare soil, road, birch forest, larch forest, water surface and buildings. Decision rules were largely based on the Ratio Vegetation Index (RVI), the Normalized Difference Water Index (NDWI) and CHM. Dynamic parameters determined the seasonal change of reflectance, such as component reflectances, LAI and sun position, obtained mainly from time series of MODIS products, including NDVI, LAI and land surface temperature (LST).

Leaf reflectance

Leaf reflectance and transmittance were measured only once, which was not sufficient to represent optical features for the entire growing season. Thanks to the PROSPECT model and changing the most sensitive input (leaf chlorophyll

content) while fixing others, seasonal leaf reflectance and transmittance could be simulated (Barry et al. 2009). Previous studies have shown that the amount of leaf chlorophyll is correlated with NDVI (Wu et al. 2008; Rulinda et al. 2011; Croft et al. 2013; Feng and Niu 2014). Therefore, we used a linear relationship between MODIS NDVI products (0.1 to 1.0) and the amount of leaf chlorophyll (10 to $100 \mu\text{g}\cdot\text{cm}^{-2}$).

Background reflectance

Seasonal variation in background reflectance was complex. However, soil moisture played a major role (Muller and Décamps 2001; Weidong et al. 2002; Whiting et al. 2004), which was then derived from TVDI (temperature vegetation dryness index) inferred from temperature and NDVI (Sandholt et al. 2002; Liang et al. 2014). TVDI is highly correlated with soil moisture (Holzman et al. 2014). Therefore, we estimated the soil reflectance as the weighted average of dry soil and wet soil reflectance, where the weights were TVDI and (1-TVDI) respectively. The background was defined as soil covered by a homogeneous shrub layer with a LAI of 0.5. Shrub leaves were assumed to have the same optical parameters as birch leaves.

Growing season

From the Landsat classification map, pure birch and larch pixels were selected to determine the beginning and final day (DOY) of the annual growing season, using the following phenology analysis.

First, MODIS time series NDVI data were fitted using a harmonic analysis (Jonsson and Eklundh 2004) to remove random noises. We referred to the maximum and minimum values of NDVI as $NDVI_{max}$ and $NDVI_{min}$.

The starting date was defined as the DOY when NDVI exceeded 20 % of $(NDVI_{max} - NDVI_{min})$ between DOY 1 and DOY 180. Similarly, the final date was the DOY when NDVI exceeded 20 % of $(NDVI_{max} - NDVI_{min})$ between DOY 180 and DOY 365.

Temporal leaf area index of individual trees

It was difficult to calculate LAI_{tree} precisely. Instead, it was possible to allocate the MODIS LAI into individual trees. Based on assumption (3), LAI_{tree} is linearly related to tree height (H_{tree}) for each species. Therefore, LAI_{tree} is a function of both species and DOY (see Equation 1).

$$LAI_{tree} = f(\text{species}) \times g(\text{DOY}) \times H_{tree} \tag{1}$$

where f is a coefficient relating H_{tree} to LAI_{tree} , which is constant for each species and g is a temporal correction factor. Plot LAI and individual tree height in field plots were used to calibrate f values for both birch or larch:

$$\sum f_i \times H_i \times (\pi R_i^2) = LAI_{plot} \times Area_{plot} \Rightarrow f = \frac{LAI_{plot} \times Area_{plot}}{\sum H_i \times (\pi R_i^2)} \tag{2}$$

For birch trees, we calibrated f as 0.25 and 0.20 for larch. From previous studies (Li et al. 2009; Liu and Jin 2013), we determined that the LAI of birch and larch varied with DOY and could be fitted with a polynomial

equation. Both species showed very similar phenology in the spring without a difference on the average (Delbart et al. 2005), so we used the MODIS LAI to calibrate the g value for both species:

$$\sum g(\text{DOY}) \times f_i \times H_i \times (\pi R_i^2) = LAI_{MODIS} \times Area_{MODIS} \Rightarrow g(\text{DOY}) = \frac{LAI_{MODIS} \times Area_{MODIS}}{\sum f_i \times H_i \times (\pi R_i^2)} \tag{3}$$

Evaluation method

Since the TreeVaW (Popescu and Wynne 2004) had not been tested in our study site, we manually segmented a few tree crowns in nine sub-plots with different tree densities in order to evaluate the accuracy of the extracted number of trees, height, location and crown radius.

We carried out four types of evaluations: (a) CCD image was used to check the pattern of simulated half-meter images; (b) Landsat images were used to check reflectance values of nadir images at the same date; (c) MODIS BRF products were used to compare simulated BRFs and (d) finally, we used four dates of Landsat images to evaluate temporal simulations.

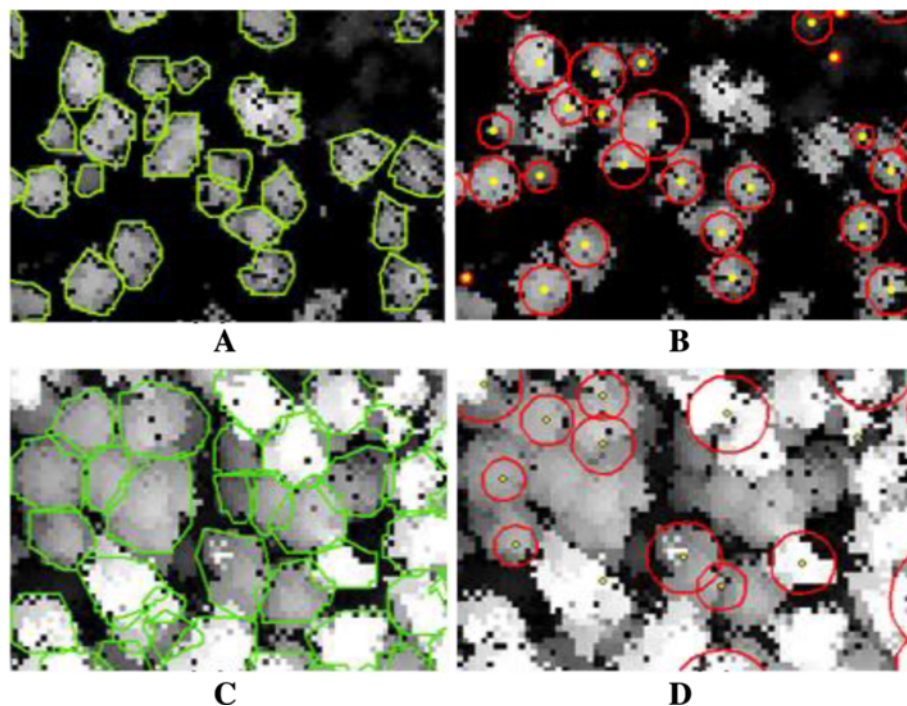
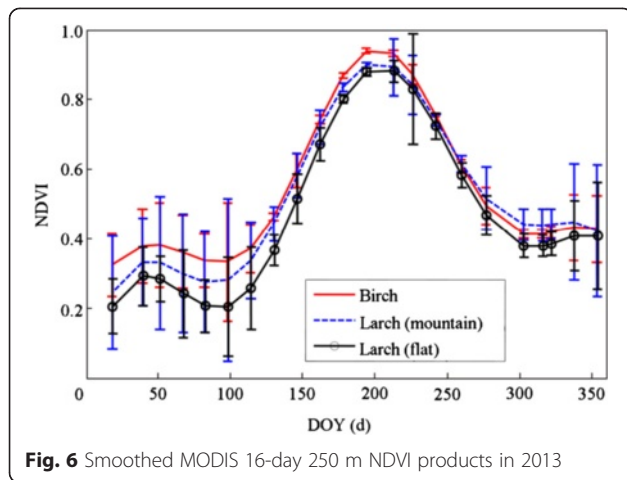


Fig. 5 Comparisons of tree segmentation between manual operation and TreeVaW in a sparse subplot (a-b) and a dense subplot (c-d); (a) and (c) are manual results; (b) and (d) are TreeVaW results



Results

Tree structure

Compared to manual segmentation, TreeVaW detected 88 % of the number of trees in sparse plots (Fig. 5a, b), but only 74 % in dense plots (Fig. 5c, d). Crown radii obtained from TreeVaW ranged from 0.59 to 0.71 m, lower than those from manual segmentation. The mean tree height error and location bias of detected trees was 0.88 and 0.91 m.

Based on regression analysis of plot data, both tree DBH and crown length (*L*) were well predicted from tree height (*H*) with coefficients of determination larger than 0.80:

$$DBH (birch) = 0.2466H^{1.5652} \quad (R^2 = 0.89) \quad (4)$$

$$DBH (larch) = 0.1639H^{1.8704} \quad (R^2 = 0.82) \quad (5)$$

$$L (birch) = 0.5475H - 0.0118 \quad (R^2 = 0.87) \quad (6)$$

$$L (larch) = 0.6551H - 0.0731 \quad (R^2 = 0.55) \quad (7)$$

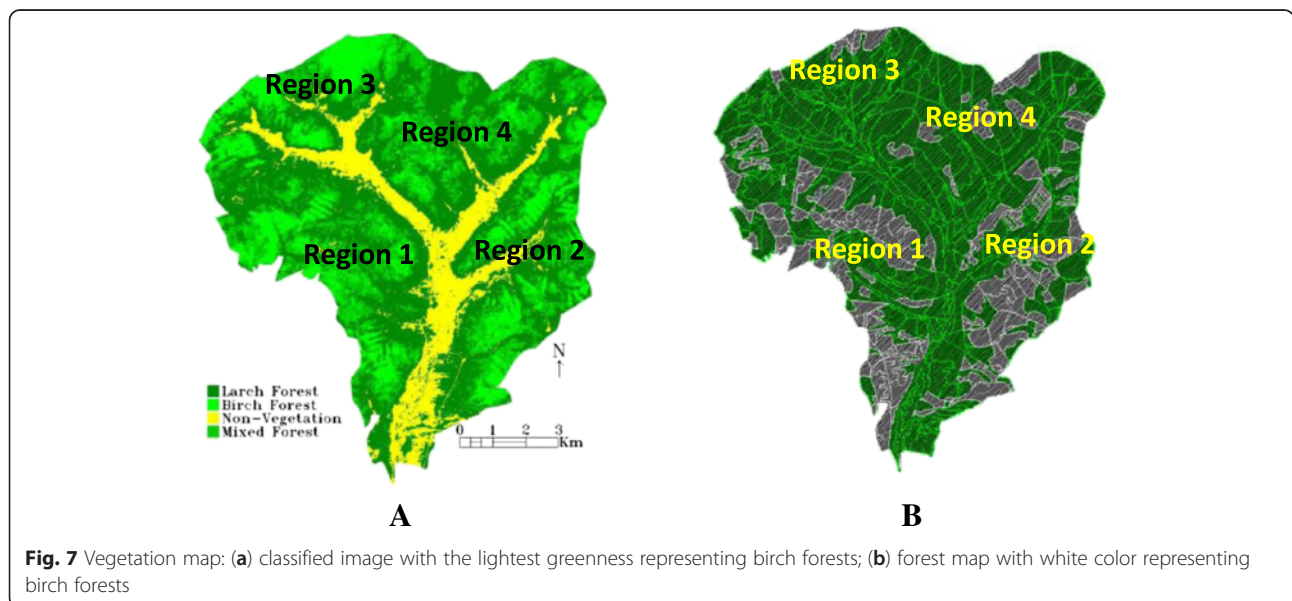
Growing season

Figure 6 shows the smoothed NDVI curves for birch and larch-dominated forests. The starting date, final date and length of the growing season were estimated as DOY 140 (May 20), 273 (Sep 3) and 130 days. During the growing season, the birch forest had higher NDVI values than larch forests, and the larch forests in the flat wetland area had significant lower NDVI values than those in mountain areas.

Land cover classification

The Landsat 8 image on May 24, 2014 was used to produce a 15 m classification map, given a suitable growing season and good image quality to distinguish birch and larch (Fig. 7a). Compared to the old forest map (Fig. 7b), the southern regions (1 and 2) visually matched much better than the northern regions (3 and 4). Fortunately, the major study area was located in regions 1 and 2, where the accuracy (around 75 %) was calculated from random sampling points. Major rules of the decision tree were the following: (1) forest vegetations = (RVI > 0 and NDWI > 0 and CHM > 2 m); (2) shrubs or grasses = (RVI > 0 and NDWI > 0 and CHM ≤ 2 m); (3) birch = ((1) and RVI > 7.0); (4) larch = ((1) and RVI ≤ 5.0); (5) mixed forests = ((1) and RVI > 5.0 and RVI ≤ 7.0).

Forest understory in the Genhe Reserve was complex but of considerable value in identifying forest types (see Table 1). Some shrubs were evergreen, while grasses shed leaves. Therefore, the vegetation detected in SPOT-6



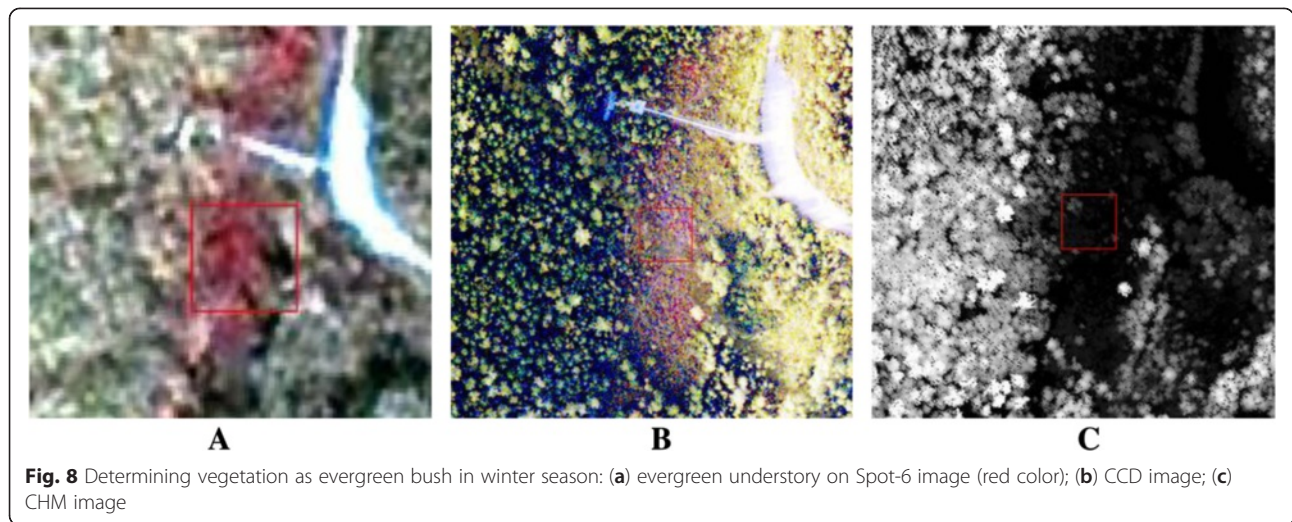


image (1 m, October) was used to define shrubs as evergreen vegetation because only evergreens had green leaves at that time of the year (Fig. 8).

Comparisons of nadir images

Simulated nadir images (0.5 m resolution) were compared to the CCD image in Fig. 9. The spatial texture and land cover difference are consistent, but the simulated forests look sparser.

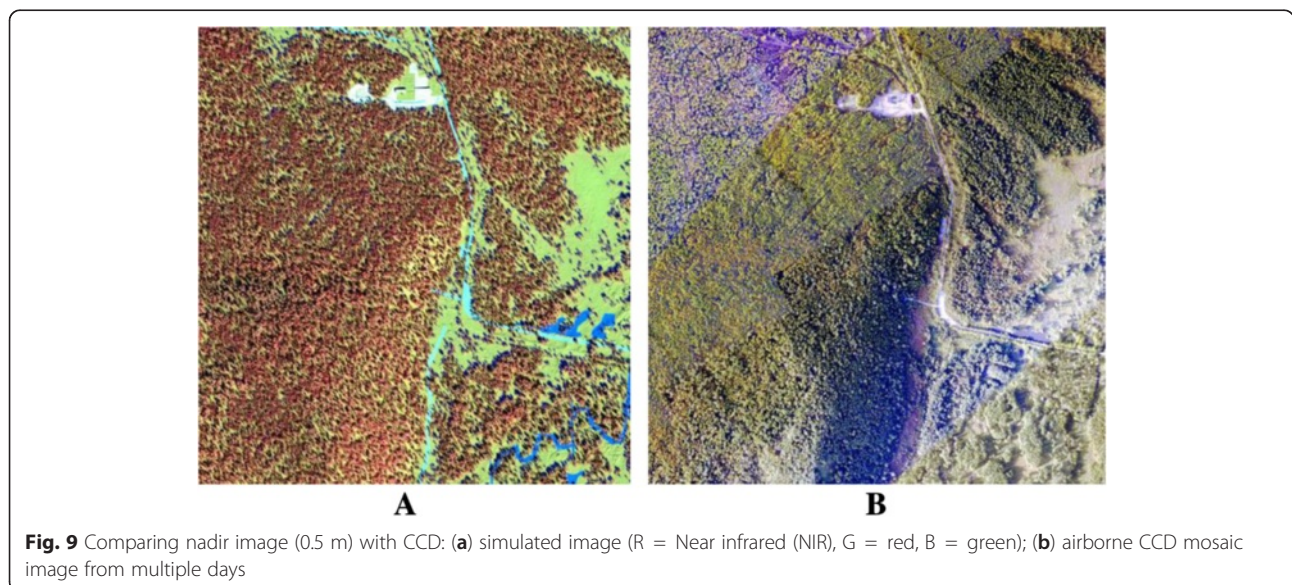
The spectral results were compared with Landsat 8 reflectance images on May 24, 2014 (Fig. 10). Both simulation and Landsat images showed typical vegetation reflectance spectra (low red reflectance and high near infrared (NIR) reflectance). Simulation results are significantly lower in blue bands (0.02 to 0.06).

Comparisons of BRF

Five pixels around the central study area showed variation in the BRF curves, used as a reference to evaluate the RAPID BRF results (Fig. 11). Generally, the simulated BRF matches the shape of MODIS BRF in spite of absolute biases in a few view directions. First, the simulated red BRF is higher than all MODIS BRFs when the view zenith angle (VZA) is between -50° and 40° . Second, in both red and NIR bands, the backscattering BRF when VZA larger than 50° , is lower than the MODIS BRF.

Temporal results

Four Landsat images were used to check the simulation ability of temporal variations; the dynamic parameters of birch and larch trees are shown in Table 2.



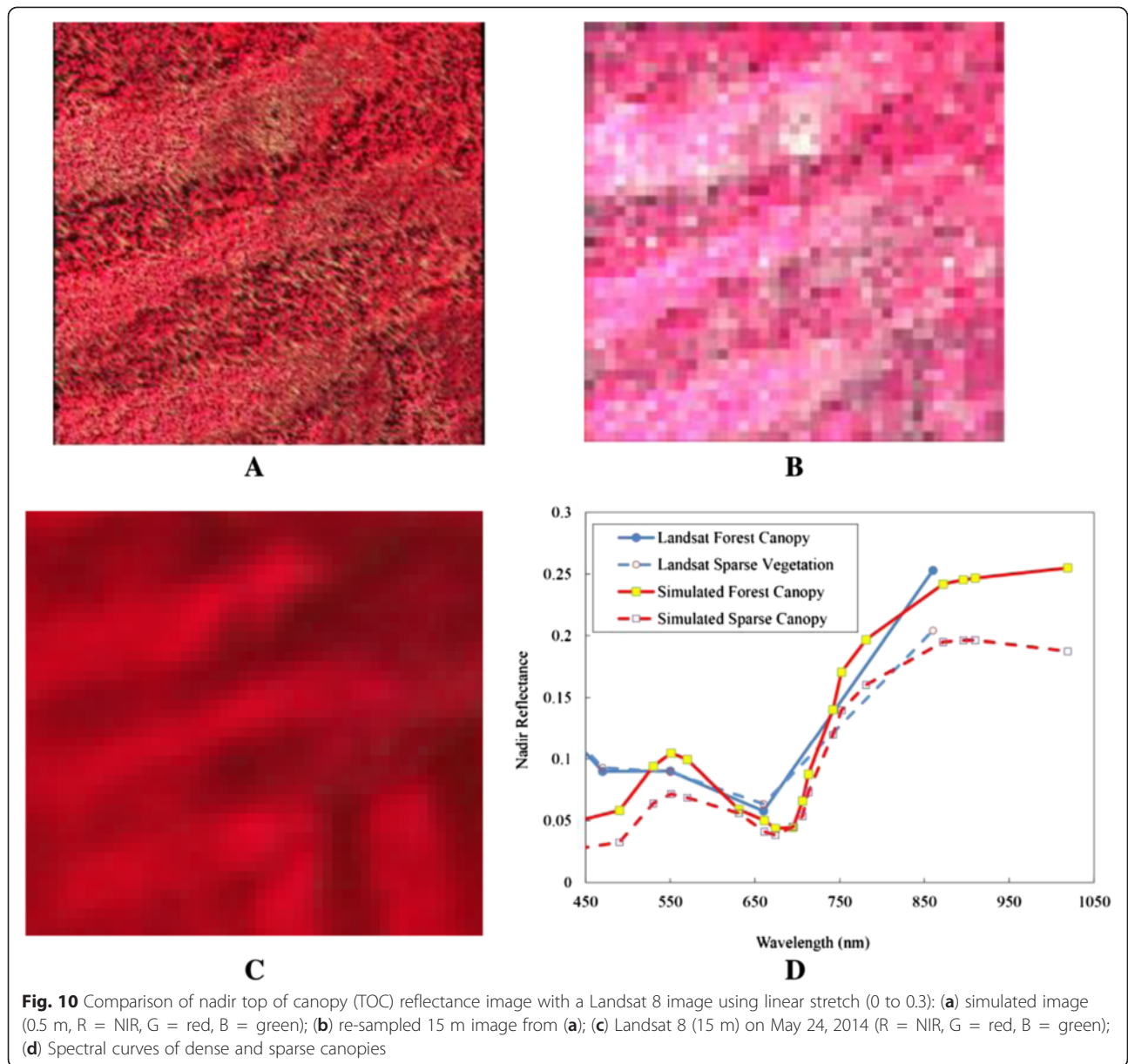


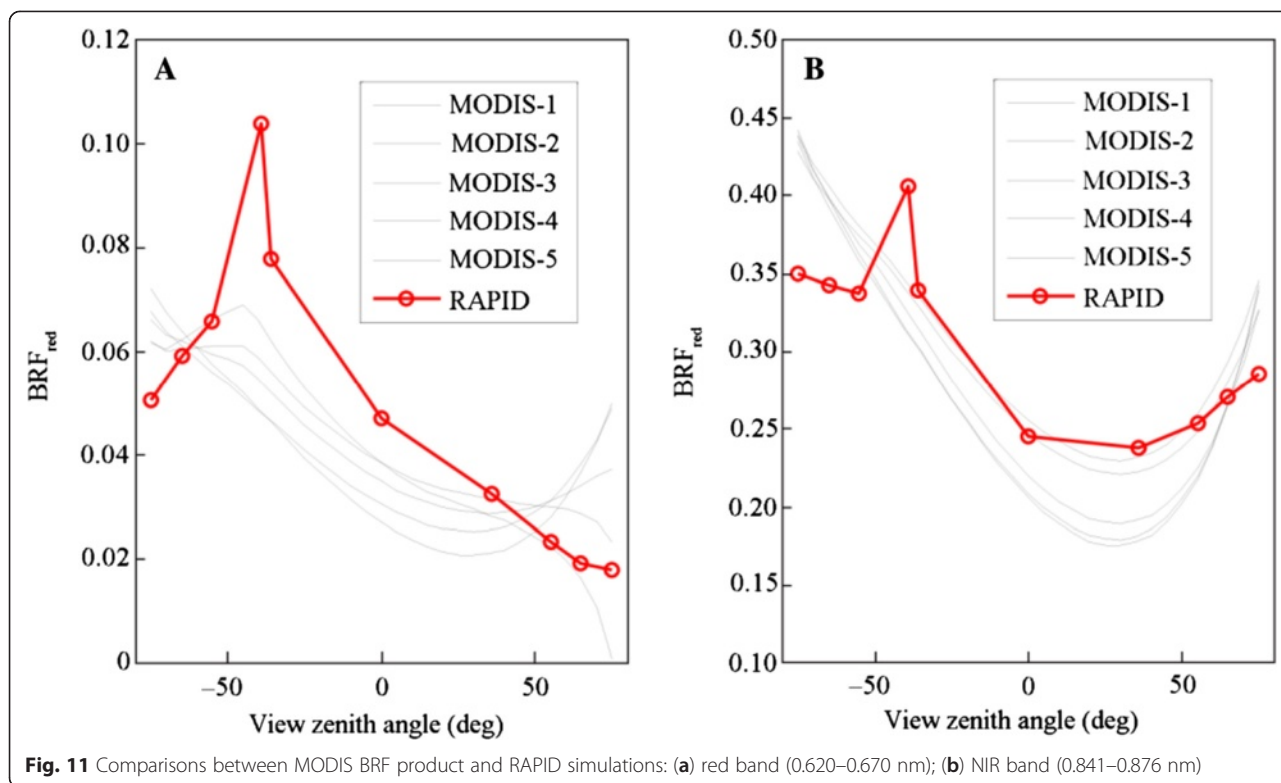
Figure 12 compares the results between simulated and real images in stripes of birch and larch forest stands (600 m by 600 m). The resolutions were 15 m except for the Landsat TM image (30 m) on September 5, 2013. The birch bands (marked as A) showed significant variation in reflectance from brown color (bare soil), red color (green canopy), pink color (dense canopy) to mixed color (discoloring canopy), reconstructed from simulated images in spite of slightly different colors. In the lower part of the Landsat ETM+ image, a black no-data area showed up, due to a sensor error (SLC-OFF). The results on Sept 5, 2013 showed larger discrepancies.

Discussion

Our main objective was to create and test how to couple lidar data and temporal optical data MODIS in order to simulate high-resolution optical satellite images. A framework was built and tested at the Genhe Forest Farm. In spite of some biases or errors, the approach successfully produced temporal images with high spatial, spectral and angular resolutions, which confirmed the possibility to fuse lidar and MODIS data.

Major contributors on simulation

The framework included four main data sources: lidar, Landsat, MODIS and field data. To drive a 3D model,



the most important inputs were 3D scenes and the inside reflectance and transmittance of 3D objects. Lidar was the first contributor to providing 3D structures of individual trees and background. Lidar-derived 3D structures were normally static, but 3D scenic objects, especially their LAI, were dynamic. Therefore, we used an allocation method to downscale MODIS LAI into each tree, a technique not found in previous studies. Landsat images were used to classify birch and larch, supporting the generation of 3D trees.

The optical parameters of 3D objects were collected in the field or obtained from existing references; these were also dynamic. Therefore, MODIS NDVI data were used to calibrate leaf chlorophyll for the PROSPECT model, which then simulated dynamic leaf reflectance and transmittance. Background soil reflectance varied over time and was difficult to obtain. An alternative is to use TVDI to adjust soil reflectance, which is a more recent idea and needs to be evaluated in any future research.

Major errors

Despite the fact that three types of evaluation on reflectance, i.e., spatial texture, BRF and Landsat simulation demonstrated the capability to simulate temporal images, quantitative validation was still missing due to lots of uncertainties in the entire workflow. We tried to address major error sources and assess their uncertainty:

- 1) 3D structure errors:

It has to be admitted that suppressed trees and irregular tree crowns are hard to detect from CHM. A previous study has shown that TreeVaW method can identify more than 95 % of the trees in planted forests but only 70 % in natural forests (Antonarakis et al. 2008). Although other detection algorithms may help improve the accuracy, the inter-comparisons between detection methods found that the correct percentage of the number of trees was generally between 50 to 90 % (Kaartinen et al. 2012). In our

Table 2 Dynamic parameters of birch or larch forests

Date	DOY	Chlorophyll content ($\mu\text{g}\cdot\text{cm}^{-2}$)	$\text{LAI}_{\text{larch}}$ ($\text{m}^2\cdot\text{m}^{-2}$)	$\text{LAI}_{\text{birch}}$ ($\text{m}^2\cdot\text{m}^{-2}$)	TVDI
May 5, 2013	125	41	$0.16 \times H_{\text{tree}}$	$0.13 \times H_{\text{tree}}$	0.61
May 24, 2014	144	52	$0.17 \times H_{\text{tree}}$	$0.18 \times H_{\text{tree}}$	0.68
June 27, 2012	179	85	$0.20 \times H_{\text{tree}}$	$0.23 \times H_{\text{tree}}$	0.91
Sept 5, 2013	248	72	$0.19 \times H_{\text{tree}}$	$0.11 \times H_{\text{tree}}$	0.62

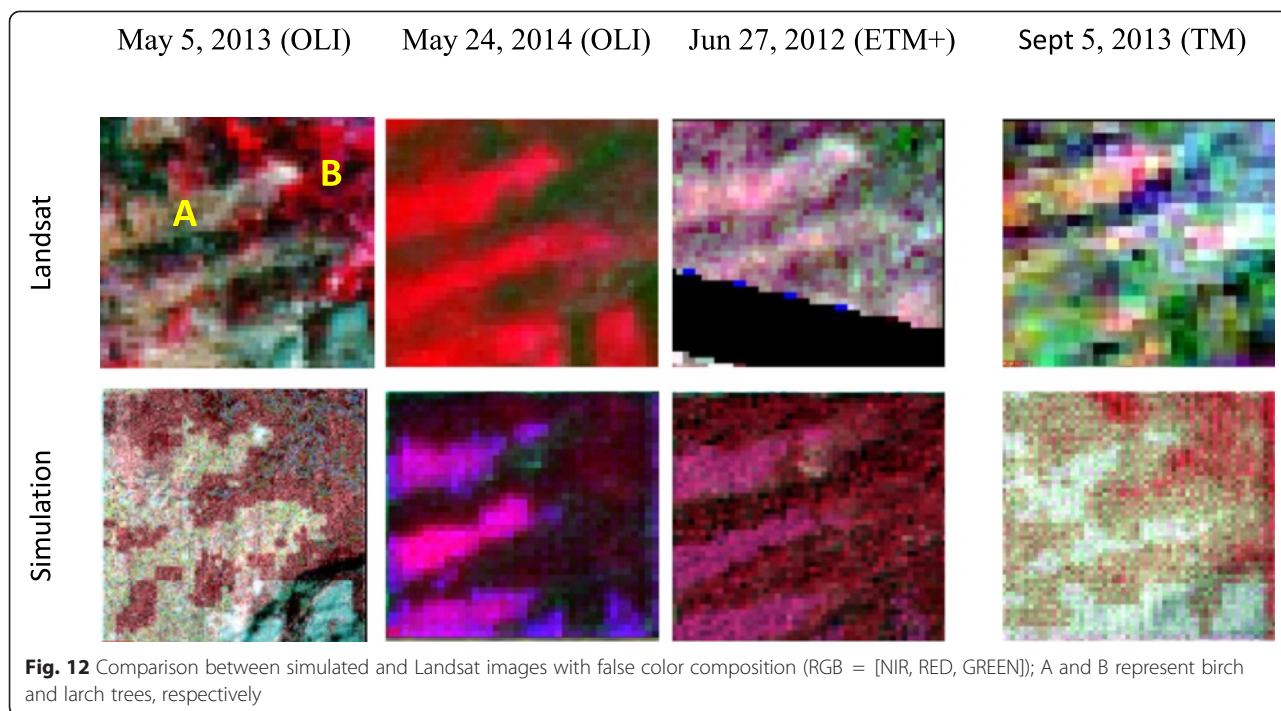


Fig. 12 Comparison between simulated and Landsat images with false color composition (RGB = [NIR, RED, GREEN]); A and B represent birch and larch trees, respectively

study, the percentage of the correct number was between 74 to 90 %, which is consistent with results above. The high level of missed detection leads to a higher clumping effect and sparser forests (Figs. 7 and 8), which then resulted in higher reflectance biases induced by background uncertainties.

2) Unknown background:

Although we classified evergreen bush, its background type and dynamic reflectance were almost unknown. Therefore, a very rude LAI of 0.5 was assumed for all understories. In fact, it is possible to retrieve forest background reflectance from satellite data (Canisius and Chen 2007; Pisek and Chen 2009; Pisek et al. 2010; Tuanmu et al. 2010; Rautiainen et al. 2011; Pisek et al. 2012). We will try these methods to inverse background reflectance in later studies. We were able to validate the TVDI-adjusted soil reflectance, although it should have directional effects. Actually, we used isotropic soil reflectance, which may explain the BRF biases with large angles in backward view directions.

3) Leaf discoloring

In September, the leaves of both birch and larch changed color. However, these changes varied even for trees of the same species, probably an effect of age, elevation or density, making it difficult to identify individual trees. Therefore, the accuracy in discoloration during the growing

season will be low. Continuous field observations are strongly suggested.

4) MODIS data uncertainty

The most recent MODIS LAI product is Collection 5 (this a version code), which has uncertainties around +/-1.0 for relatively pure pixels (Fang et al. 2012). However, considering the low resolution of MODIS pixels, the uncertainties of inversed LAIs are even larger for mixed pixels. The image matching between MODIS (1 km) and CHM (0.5 m) sounds tricky. However, as the only available product, it was used in our simulation framework. In any future study, we will use Landsat images to bridge the gap of higher resolution of LAI products (Gao et al. 2014). The BRF biases between simulation and MODIS can be partially attributed to the limitations of MODIS BRF in reconstructing higher and narrower hotspots (Huang et al. 2013b).

5) Landsat data uncertainty

Landsat images were used to compare simulated nadir reflectance and image textures. Figure 10 shows significant differences in the blue band, which can be largely explained by an atmospheric correction error because blue band reflectance should be lower after a correct removal of aerosol scatter. This atmospheric correction was carried out by using the FLAASH module of the ENVI 5.1 software, where the aerosol optical

depth and water content were only estimated from images.

Efficiency problems

RAPID is relatively fast with 3D models, but running one case (1 km) still needs four to six hours at individual tree scale on a workstation (using 10 CPU cores). We are of the opinion that it is not feasible for the generation of operational products. However, for some scientific use, focused on local areas, it may be worthwhile to obtain images with very high resolutions (spatial, spectral and angular) for research within an acceptable time frame and cost structure. Because RAPID can run at scalable resolutions, 3D scenes of dense forests can be up-scaled to regular grids with a medium resolution (e.g. 5 to 10 m), which significantly improves calculation efficiency (less than 30 min) without much loss in accuracy. Furthermore, we can create a reference table of 3D scenes, classifying a study area into fewer categories with possible combinations of DEM, understory, tree locations, tree heights and tree LAI. The corresponding reflectance images will be simulated and stored as an image database. Once the database is created, a quick search method can be used to pick up desired images based on input parameters such as DEM, understory, tree distribution and LAI. In the current framework, we only dealt with the capability of coupling simulation. Improvements will be presented in our next study.

Scale issues

Scale effect and scaling have been big issues in remote sensing community. When models or algorithms at small scales are used at large scales, they may produce certain errors, especially for non-linear models (Tao et al. 2009). Scale issues constrain the accuracy of retrieval and limit the development of remote sensing applications. In this study, MODIS LAI products at a 1 km scale were down-scaled to the level of LAI of individual trees, using lidar at a scale of only a few meters, used to coincide with the RAPID model scale. Assuming that MODIS LAI products are scale-corrected, this scaling does not change total leaf area. Since LAI_{tree} was found to be correlated with tree height, the down-scaling model should also be linear without model scale issues. In comparison with satellite images, the simulated RAPID images should also be re-sampled to coincide with the satellite scale, including the MODIS and Landsat scales. Fortunately, reflectance or radiance images are scale independent.

Using MODIS and lidar data to reconstruct 3D scenes at an individual tree scale, the RAPID model is capable of simulating time series of images at spatial scales from 0.5 m to 1 km and temporal scales of a few days. Although the 3D scene estimation is not perfect, this type of multi-

scale optical image dataset will be useful to support the understanding of scale problems.

Conclusions

We presented a simulation framework which links lidar with optical images to produce series of temporal images. The study provides a proof-of-concept approach to link lidar data in the parameterization of a RAPID model for temporal image reconstruction in forest dominated areas. Demonstrations were applied at the Genhe Forest Farm, a remote forest reserve in China. Evaluations on nadir reflectance, spatial textures and BRF confirmed that 3D simulation provides an insight look into how images vary over time. Many uncertainties were identified, which can be expected to be reduced in any future study. Strategies to improve efficiency are possible and discussed.

Competing interests

The authors declare that they have no competing interests.

Authors' contributions

HH is the major and contact author for most work. JL processed a small part of the data. Both authors read and approved the final manuscript.

Acknowledgements

The authors gratefully acknowledge the Chinese National Basic Research Program (2013CB733401) and the Chinese Natural Science Foundation Project (41171278).

Received: 28 February 2015 Accepted: 18 June 2015

Published online: 26 June 2015

References

- Adams T, Beets P, Parrish C (2012) Extracting more data from LiDAR in forested areas by analyzing waveform shape. *Remote Sens* 4(3):682–702. doi:10.3390/rs4030682
- Ahl DE, Gower ST, Burrows SN, Shabanov NV, Myneni RB, Knyazikhin Y (2006) Monitoring spring canopy phenology of a deciduous broadleaf forest using MODIS. *Remote Sens Environ* 104(1):88–95. doi:10.1016/j.rse.2006.05.003
- Antonarakis AS, Richards KS, Brasington J, Bithell M, Muller E (2008) Retrieval of vegetative fluid resistance terms for rigid stems using airborne lidar. *J Geophys Res* 113(G2):G02S07. doi:10.1029/2007JG000543
- Arno J, Escola A, Valles JM, Llorens J, Sanz R, Masip J, Palacin J, Rosell-Polo JR (2013) Leaf area index estimation in vineyards using a ground-based LiDAR scanner. *Precision Agric* 14(3):290–306. doi:10.1007/s11119-012-9295-0
- Barbier N, Proisy C, Vega C, Sabatier D, Coutron P (2011) Bidirectional texture function of high resolution optical images of tropical forest: An approach using LiDAR hillshade simulations. *Remote Sens Environ* 115(1):167–179. doi:10.1016/j.rse.2010.08.015
- Barry KM, Newnham GJ, Stone C (2009) Estimation of chlorophyll content in *Eucalyptus globulus* foliage with the leaf reflectance model PROSPECT. *Agr Forest Meteorol* 149(6–7):1209–1213. http://dx.doi.org/10.1016/j.agrformet.2009.01.005
- Canisius F, Chen JM (2007) Retrieving forest background reflectance in a boreal region from Multi-angle Imaging SpectroRadiometer (MISR) data. *Remote Sens Environ* 107(1–2):312–321. doi:10.1016/j.rse.2006.07.023
- Chen G, Wulder MA, White JC, Hilker T, Coops NC (2012) Lidar calibration and validation for geometric-optical modeling with Landsat imagery. *Remote Sens Environ* 124(0):384–393. http://dx.doi.org/10.1016/j.rse.2012.05.026
- Croft H, Chen JM, Zhang Y, Simic A (2013) Modelling leaf chlorophyll content in broadleaf and needle leaf canopies from ground, CASI, Landsat TM 5 and MERIS reflectance data. *Remote Sens Environ* 133(0):128–140. http://dx.doi.org/10.1016/j.rse.2013.02.006
- Delbart N, Kergoat L, Le Toan T, Lhermitte J, Picard G (2005) Determination of phenological dates in boreal regions using normalized difference water index. *Remote Sens Environ* 97(1):26–38. doi:10.1016/j.rse.2005.03.011

- Fang H, Wei S, Liang S (2012) Validation of MODIS and CYCLOPES LAI products using global field measurement data. *Remote Sens Environ* 119:43–54. doi:10.1016/j.rse.2011.12.006
- Feng M, Niu Z (2014) Chlorophyll content retrieve of vegetation using Hyperion data based on empirical models. *Remote Sens Land Resour* 26(1):71–77. doi:10.6046/gtzyyg.2014.01.13
- Gao F, Anderson MC, Kustas WP, Houborg R (2014) Retrieving leaf area index from landsat using MODIS LAI products and field measurements. *IEEE Geosci Remote Sens Lett* 11(4):773–777. doi:10.1109/Lgrs.2013.2278782
- Gao F, Masek J, Schwaller M, Hall F (2006) On the blending of the Landsat and MODIS surface reflectance: predicting daily Landsat surface reflectance. *IEEE Trans Geosci Remote Sens* 44(8):2207–2218. doi:10.1109/tgrs.2006.872081
- García Millán VE, Sánchez-Azofeifa A, Málvarez García GC, Rivard B (2014) Quantifying tropical dry forest succession in the Americas using CHRIS/PROBA. *Remote Sens Environ* 144(0):120–136. http://dx.doi.org/10.1016/j.rse.2014.01.010
- Hilker T, Wulder MA, Coops NC, Seitz N, White JC, Gao F, Masek JG, Stenhouse G (2009) Generation of dense time series synthetic Landsat data through data blending with MODIS using a spatial and temporal adaptive reflectance fusion model. *Remote Sens Environ* 113(9):1988–1999. doi:10.1016/j.rse.2009.05.011
- Holzman ME, Rivas R, Bayala M (2014) Subsurface soil moisture estimation by VI-LST method. *IEEE Geosci Remote Sens Lett* 11(11):1951–1955. doi:10.1109/Lgrs.2014.2314617
- Huang H, Qin W, Liu Q (2013a) RAPID: a radiosity applicable to porous individual objects for directional reflectance over complex vegetated scenes. *Remote Sens Environ* 132:221–237. doi:10.1016/j.rse.2013.01.013
- Huang X, Jiao Z, Dong Y, Zhang H, Li X (2013b) Analysis of BRDF and albedo retrieved by kernel-driven models using field measurements. *IEEE J Selected Topics Appl Earth Observ Remote Sens* 6(1):149–161. doi:10.1109/Jstars.2012.2208264
- Inglada J, Hagolle O, Dedieu G (2011) A framework for the simulation of high temporal resolution image series. Paper presented at the IEEE International Geoscience and Remote Sensing Symposium (IGARSS), 24–29 July 2011
- Jacquemoud S, Verhoef W, Baret F, Bacour C, Zarco-Tejada PJ, Asner GP, François C, Ustin SL (2009) PROSPECT + SAIL models: a review of use for vegetation characterization. *Remote Sens Environ* 113(Supplement 1 (0)):S56–S66. http://dx.doi.org/10.1016/j.rse.2008.01.026
- Jonsson P, Eklundh L (2004) TIMESAT - a program for analyzing time-series of satellite sensor data. *Comput Geosci* 30(8):833–845. doi:10.1016/j.cageo.2004.05.006
- Kaartinen H, Hyyppä J, Yu X, Vastaranta M, Hyyppä H, Kukko A, Holopainen M, Heipke C, Hirschmugl M, Morsdorf F, Næsset E, Pitkänen J, Popescu S, Solberg S, Wolf BM, Wu J-C (2012) An international comparison of individual tree detection and extraction using airborne laser scanning. *Remote Sensing* 4(4):950–974
- Kobayashi H, Suzuki R, Kobayashi S (2007) Reflectance seasonality and its relation to the canopy leaf area index in an eastern Siberian larch forest: Multi-satellite data and radiative transfer analyses. *Remote Sens Environ* 106(2):238–252. doi:10.1016/j.rse.2006.08.011
- Li GZ, Wang HX, Zhu JJ (2009) Monthly changes of leaf area index and canopy openness of *Larix olgensis* in mountainous regions in east Liaoning province. *J Northeast Forestry Univ* 37(7):13
- Liang L, Zhao S-h, Qin Z-h, He K-x, Chen C, Luo Y-x, Zhou X-d (2014) Drought change trend using MODIS TVDI and its relationship with climate factors in china from 2001 to 2010. *J Integr Agric* 13(7):1501–1508. http://dx.doi.org/10.1016/S2095-3119(14)60813-3
- Liu ZL, Jin GZ (2013) Estimation of leaf area index of secondary *Betula platyphylla* forest in Xiaoxing'an Mountains. *Acta Ecologica Sinica* 33(8):9
- Lucas RM, Lee AC, Williams ML (2006) Enhanced simulation of radar backscatter from forests using LiDAR and optical data. *IEEE Trans Geosci Remote Sens* 44(10):2736–2754. doi:10.1109/tgrs.2006.881802
- Lunetta RS, Johnson DM, Lyon JG, Crowell J (2004) Impacts of imagery temporal frequency on land-cover change detection monitoring. *Remote Sens Environ* 89(4):444–454. doi:10.1016/j.rse.2003.10.022
- Masek JG, Huang C, Wolfe R, Cohen W, Hall F, Kutler J, Nelson P (2008) North American forest disturbance mapped from a decadal Landsat record. *Remote Sens Environ* 112(6):2914–2926. doi:10.1016/j.rse.2008.02.010
- Montesano P, Cook B, Sun G, Simard M, Nelson R, Ranson K, Zhang Z, Luthcke S (2013) Achieving accuracy requirements for forest biomass mapping: a spaceborne data fusion method for estimating forest biomass and LiDAR sampling error. *Remote Sens Environ* 130:153–170. doi:10.1016/j.rse.2012.11.016
- Mu X, Zhang Q, Liu Q, Pang Y, Hu K (2015) A study on typical forest biomass mapping technology of great khingan using airborne laser scanner data. *Remote Sens Technol Appl* 30(2):220–225
- Muller E, Décamps H (2001) Modeling soil moisture–reflectance. *Remote Sens Environ* 76(2):173–180. http://dx.doi.org/10.1016/S0034-4257(00)00198-X
- Nitze I, Barrett B, Cavkwell F (2015) Temporal optimisation of image acquisition for land cover classification with Random Forest and MODIS time-series. *Int J Appl Earth Observ Geoinformation* 34:136–146. doi:10.1016/j.jag.2014.08.001
- Pisek J, Chen JM (2009) Mapping forest background reflectivity over North America with Multi-angle Imaging SpectroRadiometer (MISR) data. *Remote Sens Environ* 113(11):2412–2423. doi:10.1016/j.rse.2009.07.003
- Pisek J, Chen JM, Miller JR, Freemantle JR, Peltoniemi JJ, Simic A (2010) Mapping forest background reflectance in a boreal region using multiangle compact airborne spectrographic imager data. *IEEE Trans Geosci Remote Sens* 48(1):499–510. doi:10.1109/tgrs.2009.2024756
- Pisek J, Rautiainen M, Heiskanen J, Mottus M (2012) Retrieval of seasonal dynamics of forest understory reflectance in a Northern European boreal forest from MODIS BRDF data. *Remote Sens Environ* 117:464–468. doi:10.1016/j.rse.2011.09.012
- Popescu SC, Wynne RH (2004) Seeing the trees in the forest: using lidar and multispectral data fusion with local filtering and variable window size for estimating tree height. *Photogrammetric Eng Remote Sens* 70(5):589–604
- Rautiainen M, Lang M, Mottus M, Kuusk A, Nilson T, Kuusk J, Lökk T (2008) Multi-angular reflectance properties of a hemiboreal forest: An analysis using CHRIS PROBA data. *Remote Sens Environ* 112(5):2627–2642. http://dx.doi.org/10.1016/j.rse.2007.12.005
- Rautiainen M, Mottus M, Heiskanen J, Ajujarvi A, Majasalmi T, Stenberg P (2011) Seasonal reflectance dynamics of common understory types in a northern European boreal forest. *Remote Sens Environ* 115(12):3020–3028. doi:10.1016/j.rse.2011.06.005
- Rulinda CM, Bijker W, Stein A (2011) The chlorophyll variability in Meteosat derived NDVI in a context of drought monitoring. *Procedia Environ Sci* 3(0):32–37. http://dx.doi.org/10.1016/j.proenv.2011.02.007
- Sandholt I, Rasmussen K, Andersen J (2002) A simple interpretation of the surface temperature/vegetation index space for assessment of surface moisture status. *Remote Sens Environ* 79(2–3):213–224. http://dx.doi.org/10.1016/S0034-4257(01)00274-7
- Schaaf CB, Strahler AH (1994) Validation of bidirectional and hemispherical reflectances from a geometric-optical model using ASAS imagery and pyranometer measurements of a spruce forest. *Remote Sens Environ* 49(2):138–144. http://dx.doi.org/10.1016/0034-4257(94)90050-7
- Sharma RC, Kajiwara K, Honda Y (2013) Estimation of forest canopy structural parameters using kernel-driven bi-directional reflectance model based multi-angular vegetation indices. *ISPRS J Photogrammetry Remote Sens* 78:50–57. doi:10.1016/j.isprsjprs.2012.12.006
- Tao X, Yan B, Wang K, Wu D, Fan W, Xu X, Liang S (2009) Scale transformation of Leaf Area Index product retrieved from multiresolution remotely sensed data: analysis and case studies. *Int J Remote Sens* 30(20):5383–5395. doi:10.1080/01431160903130978
- Tuanmu M-N, Vina A, Bearer S, Xu W, Ouyang Z, Zhang H, Liu J (2010) Mapping understory vegetation using phenological characteristics derived from remotely sensed data. *Remote Sens Environ* 114(8):1833–1844. doi:10.1016/j.rse.2010.03.008
- Wang JD, Zhang LX, Liu QH, Zhang B, Yin Q (2008) The spectrum knowledge database of typical land surface objects in China. Science Press, Beijing
- Wanner W, Li X, Strahler AH (1995) On the derivation of kernels for kernel-driven models of bidirectional reflectance. *J Geophys Res* 100(D10):21077–21089. doi:10.1029/95JD02371
- Weidong L, Baret F, Xingfa G, Qingxi T, Lanfen Z, Bing Z (2002) Relating soil surface moisture to reflectance. *Remote Sens Environ* 81(2–3):238–246. http://dx.doi.org/10.1016/S0034-4257(01)00347-9
- Whiting ML, Li L, Ustin SL (2004) Predicting water content using Gaussian model on soil spectra. *Remote Sens Environ* 89(4):535–552. http://dx.doi.org/10.1016/j.rse.2003.11.009
- Wu C, Niu Z, Tang Q, Huang W (2008) Estimating chlorophyll content from hyperspectral vegetation indices: Modeling and validation. *Agr Forest Meteorol* 148(8–9):1230–1241. http://dx.doi.org/10.1016/j.agrformet.2008.03.005
- Wu M-Q, Wang J, Niu Z, Zhao Y-Q, Wang C-Y (2012) A model for spatial and temporal data fusion. *J Infrared Millimeter Waves* 31(1):80–84
- Xiao C-W, Janssens IA, Curriel Yuste J, Ceulemans R (2006) Variation of specific leaf area and upscaling to leaf area index in mature Scots pine. *Trees* 20(3):304–310. doi:10.1007/s00468-005-0039-x
- Xu G-c, Pang Y, Li Z-y, Zhao K-r, Liu L-x (2013) The changes of forest canopy spectral reflectance with seasons in Xiaoxing'anling. *Spectrosc Spectral Anal* 33(12):3303–3307